島根大学学術情報リポジトリ
SWAN
Shimane University Web Archives of kNowledge

Title

Improvement of the structural properties and environmental stability of flexible InSb thin films by dopant-assisted crystallization

Author(s)

Nishimoto N, Fujihara J.

Journal

Applied Physics A 2022; 128: 550 (2022)

Published

2022

URL（The Version of Record）

https://doi.org/10.1007/s00339-022-05694-8

この論文は出版社版でありません。

引用の際には出版社版をご確認のうえご利用ください。

This version of the article has been accepted for publication,

but is not the Version of Record.

Improvement of the structural properties and environmental stability of flexible InSb thin films by dopant-assisted crystallization

Naoki Nishimoto[1,*], Junko Fujihara[2]

[1] Department of Research Planning and Coordination, Shimane Institute for Industrial Technology, 1 Hokuryo, Matsue, Shimane 690-0816, Japan

ORCID: 0000-0002-5854-7848

[2] Department of Legal Medicine, Shimane University Faculty of Medicine, 89-1 Enya, Izumo, Shimane 693-8501, Japan

ORCID: 0000-0001-5359-5181

[*] **Corresponding author:**

Naoki Nishimoto

E-mail: nishimoto.su2010@gmail.com

Author contributions

Conceptualization: Naoki Nishimoto; Investigation and data curation: Naoki Nishimoto, Junko Fujihara; Formal analysis: Naoki Nishimoto; Funding acquisition: Junko Fujihara; Writing – original draft preparation: Naoki Nishimoto; Writing – review and editing: Junko Fujihara

Acknowledgements

This work was supported by JSPS KAKENHI Grants-in-Aid for Scientific Research (B) (grant number 21H03212) and by the “Shimane University Support Programs for Young Female Researchers” under MEXT “Initiative for Realizing Diversity in the Research Environment (Collaboration Type)” to Junko Fujihara.

Abstract

In this study, InSb and $InSb_{1-x}Bi_x$ (x = 0.01, 0.02, and 0.03) thin films were grown on quartz substrates and polyimide (PI) films by multi-cathode radio frequency magnetron sputtering. The effects of Bi doping on the structural properties, stacking-fault probabilities, and environmental resistance were investigated. The properties of the InSb/PI were inferior to those of the InSb/quartz because of the structural disorder in the InSb/PI which disrupted the (111)-oriented growth, and the preferred orientation was (220). However, the crystallinities of the Bi-doped InSb/PI were comparable with that of the InSb/quartz. The structural disorder was suppressed with the change in the preferred orientation from (220) to (111) as the Bi content x was increased, and the stacking-fault probability of $InSb_{0.97}Bi_{0.03}$/PI was similar to that of the InSb/quartz. Furthermore, the environmental stability of the InSb thin film was enhanced by Bi doping. These findings will support innovation in semiconductor fabrication and will help to decrease the environmental burden of these materials.

Keywords

InSbBi; Sputtering; X-ray diffraction; Stacking-fault; Chemical stability

Statements and Declarations

Competing Interests: There are no conflicts of interest to declare.

1 Introduction

The Sustainable Development Goals (SDGs) are 17 global goals proposed by the United Nations to achieve environmentally friendly, sustainable growth [1]. To achieve the SDGs, the semiconductor industry must innovate its fabrication processes, decrease its environmental burden, and advance the use of renewable energy [2,3]. Technological development for improving the low-temperature fabrication and environmental resistance of semiconductor thin films will help to meet these goals. Low-temperature fabrication techniques reduce CO_2 production and allow flexible substrates with low heat resistance (e.g., resin, or plastic) to be used, which means that various devices can be miniaturized and their power consumption reduced [4,5]. Increasing the environmental resistance of semiconductor materials reduces their environmental burden because most of these materials are toxic [6–8].

High-quality thin films are difficult to obtain using current mass production techniques at low growth temperatures because the semiconductor thin films produced as polycrystalline. Consequently, advances in low-temperature fabrication techniques using existing mass production techniques and materials science approaches will contribute to the innovation of fabrication processes. For example, growth surfactants encourage film growth at low temperatures and allow control on the crystallinity of semiconductor thin

films. Kamiko et al. reported that a Ag surfactant suppresses the surface roughness and controls the crystallinity of TiO_2 semiconductor thin films [9]. Schmidt et al. reported that smooth, pseudomorphically strained Ge thin films can be obtained on SiGe(001) virtual substrates by using an Sb surfactant for growing group IV semiconductors [10].

InSb has highest electron mobility (78,000 cm^2/Vs) among compound semiconductors and its physical properties have been studied extensively [11–14]. InSb thin films grown at low temperatures retain the properties required for electronic devices, even if the thin film is polycrystalline. We have revealed that Ga and N improve the electrical properties in InSb thin films grown on polyimide (PI) films using radio frequency (RF) magnetron sputtering by increasing the grain size and decreasing the defect density [4,11]. However, in those studies, the chemical stability was unchanged by adding Ga and N, and the structural property analysis was insufficient. Therefore, the effect of other dopants/surfactants and the structural analysis method for flexible thin films needs to be discussed.

Bi has been proposed as a growth surfactant for group III-V compound semiconductors [15–17]. Bi surfactants decrease the defect density, increase the photoluminescence intensity, and control the crystallinity in GaAs- and GaP-based thin films. However, the effect of Bi doping in InSb thin films grown by sputtering has not

been reported. The stacking-fault probability of face-centered-cubic (fcc) metals is often estimated by X-ray diffraction (XRD) measurements [18,19], although this analysis method has hardly been used in semiconductor thin films [20] and has never been used for flexible semiconductor thin films. In the present research, InSb and InSbBi thin films are grown on quartz substrates and PI films by multi-cathode RF magnetron sputtering. The doping effects of Bi on the structural properties, stacking-fault probabilities estimated by XRD, and environmental resistance of InSb thin films are investigated.

2 Materials and Methods

2.1 Growth of InSb and $InSb_{1-x}Bi_x$ thin films

InSb and $InSb_{1-x}Bi_x$ thin films were grown by multi-cathode RF magnetron sputtering (HSR351-L, Shimadzu Industrial Systems) on quartz substrates and 125-µm-thick PI films (Kapton, DUPONT-TORAY), which are flexible, heat and chemical resistant. Substrate surfaces were cleaned by reverse sputtering (atmosphere: Ar; temperature: room temperature; pressure: 0.3 Pa; RF power: 30 W; time: 10 min). The growth temperature was 320 °C, the growth pressure was 0.5 Pa, and the sputtering gas was Ar. The growth times were adjusted according to the number of sputtering targets so that the same film thicknesses was obtained for all samples. The RF power for all targets

was 80 W. Three $In_{0.5}Sb_{0.5}$ targets (2-in.-diameter disk of 3N purity) were used in the growth of InSb thin films (one $In_{0.5}Sb_{0.5}$ target: growth time 30 min; two $In_{0.5}Sb_{0.5}$ targets: growth time 15 min; three $In_{0.5}Sb_{0.5}$ targets: growth time 10 min). One $In_{0.5}Sb_{0.47}Bi_{0.03}$ target (2-in.-diameter disk of 3N purity) and two $In_{0.5}Sb_{0.5}$ targets were used to control Bi content x during the growth of the $InSb_{1-x}Bi_x$ thin films (one $In_{0.5}Sb_{0.47}Bi_{0.03}$ target: growth time 30 min; one $In_{0.5}Sb_{0.47}Bi_{0.03}$ target and one $In_{0.5}Sb_{0.5}$ target: growth time 15 min; one $In_{0.5}Sb_{0.47}Bi_{0.03}$ target and two $In_{0.5}Sb_{0.5}$ targets: growth time 10 min).

2.2 Characterization

Film compositions were measured by X-ray fluorescence (XRF; ZSX Primus IV, Rigaku), and film thicknesses were determined from the calculated deposition amounts using the fundamental parameter (FP) method based on XRF intensity. In addition to microscopic Raman scattering spectroscopy with a He-Ne laser (633 nm) as the excitation source (JRS-SYS2000, JEOL), crystal structures were characterized by XRD using $CuK\alpha_1$ radiation with a multilayer mirror in the incident beam line (SmartLab XE, Rigaku). Grain sizes were determined by analyzing XRD patterns with the direct derivation method based on the whole-powder-pattern fitting procedure using the FP method (SmartLab Studio II software package, Rigaku) [21]. Surface morphologies were

observed by dynamic-mode atomic force microscopy (NaioAFM, Nanosurf AG) on an anti-vibration table (Isostage, Nanosurf AG).

2.3 Chemical stability

InSb and InSbBi thin films were immersed in 0.1 M sodium acetate buffer (1.5 mL, pH 5), according to our previous studies showing that In in thin films eluted to a greater extent in sodium acetate buffer than in 0.1 M tris buffer (pH 9) [4,11]. On days 1, 3, 7, and 14, the solution (0.5 mL) was collected and acidified with 1 N HNO_3 (4.5 mL). Following collection, the 0.5 mL of sodium acetate buffer was supplemented to the immersed solution. The In concentrations in the solutions were measured by microwave plasma-atomic emission spectrometry (MP-AES; Agilent 4200 MP-AES, Agilent Technologies) equipped with an inert nebulizer (OneNeb, Agilent Technologies) and a double-pass glass cyclonic spray chamber (Agilent Technologies).

2.4 Cytotoxicity assay

To prepare the test solution, InSb/PI and InSbBi/PI films were soaked in Roswell Park Memorial Institute 1640 medium (20 mL) for 24 h at 37 °C. L929 cells were supplied by the RIKEN BioResource Research Center through the national Bio-Resource Project

of the Ministry of Education, Sports, Science and Technology (MEXT), Japan. Cells were cultured at 37 °C, 5% CO_2, and >95% humidity. Roswell Park Memorial Institute 1640 containing 10% fetal bovine serum, 5 μM 2-mercaptoethanol, and 10 U/mL penicillin was used as the culture medium. Cells were plated in a six-well plate at a density of 5×10^3 cells/well. After 24 h, the culture medium was replaced with the test solution (1 mL) and incubated for 24 h. Cells were washed with phosphate-buffered saline and Live/Dead cell staining solution (Takara Bio) was added. After 30 min, cells were washed three times with phosphate-buffered saline and imaged with a fluorescence microscope (EVOS, Thermo Fisher Scientific) using a filter cube for GFP and Texas Red.

3 Results and Discussion

3.1 Thin film properties

The film thickness was obtained from the InSb density (= 5.78 g/cm^3) and the deposition amounts measured in the thin films (≈ 3.7×10^{-4} g/cm^2) because the Bi content in the $In_{0.5}Sb_{0.47}Bi_{0.03}$ sputtering target was low. The thin films were nearly stoichiometric and the film thickness was 640 nm regardless of the growth conditions. This result indicated that growth rate was controlled by adjusting the growth time for the number of sputtering targets. The growth rates were 21.3 nm/min for one sputtering target, 42.6

nm/min for two sputtering targets, and 64.0 nm/min for three sputtering targets. The Bi content x in the $InSb_{1-x}Bi_x$ thin films grown for 21.3, 42.6, and 64.0 nm/min was 0.03, 0.02, and 0.01, respectively. These values were low compared with the Bi content in the $In_{0.5}Sb_{0.47}Bi_{0.03}$ sputtering target because the sputtering rate of Bi is lower than that of Sb [22].

The XRD patterns of the thin films are shown in Fig. 1. In the growth on quartz substrates (Fig. 1a and b), the thin films were polycrystalline with a (111) preferred orientation regardless of the growth rate and Bi content x. The diffraction intensities were increased by Bi doping, although Bi clusters were formed at Bi content $x = 0.03$ (insets (i) and (ii) in Fig. 1b). In contrast, the growth rate and Bi content x strongly affected the XRD patterns of the thin films grown on PI films (Fig. 1c and d). InSb/PI were polycrystalline thin films with a (220) preferred orientation and the diffraction intensities increased with the growth rate (Fig. 1c). Furthermore, the preferred orientation was changed from (220) to (111) as the Bi content x increased (Fig. 1d).

The surface migration of source materials on PI films is lower than that on quartz substrates because PI films have a rough, activated surface owing to the cleaning by reverse sputtering [23]. Hence, the source material supply was insufficient for the formation of InSb crystal nuclei during growth of the InSb/PI at low growth rates. The

effect was also observed in the preferred orientation of the InSb/PI. Although the InSb/PI showed a preferred orientation of (220) (Fig. 1c), the diamond and zinc-blende structures, which are obtained by translation of the fcc lattice, are easily oriented to (111) [24–26]. Zhang et al. reported that in the solid phase growth of polysilicon, defect formation may have disturbed (111)-oriented growth at low annealing temperatures (low growth driving force) [27]. The preferred orientation of the $InSb_{1-x}Bi_x$/PI gradually changed from (220) to (111) as the Bi content x increased (Fig. 1d). The XRD pattern of the $InSb_{0.97}Bi_{0.03}$/PI was similar to those of thin films grown on the quartz substrate, even though Bi clusters were formed in the $InSb_{0.97}Bi_{0.03}$/PI (inset (iii) in Fig. 1d). Thus, Bi assisted the growth of InSb thin films.

Fig. 2 shows the Raman spectra of the thin films. The red solid lines are the fitted curves of the InSb transverse optical (TO) and longitudinal optical (LO) mode peaks. In the zinc-blende structure, the TO mode is allowed for scattering from the (110) and (111) orientations, whereas the LO mode is allowed for scattering from the (001) and (111) orientations [28]. In the region indicated with an asterisk, from 70 to 150 cm^{-1}, peaks originating from structural disorder were observed (green fitted curves). The peaks around 140, 120, and 100 cm^{-1} were assigned to the A_{1g} mode of the Sb cluster, the longitudinal acoustic mode of InSb, and the amorphous components, respectively [11].

The results of the curve fitting analysis of the Raman spectra are shown in Table 1. A narrow full width at half-maximum (FWHM) was obtained at a low growth rate in the InSb/quartz (Fig. 2a and Table 1a), indicating high crystallinity. Increasing the Bi content x resulted in a narrower FWHM for the InSb TO mode and a larger $I_{\mathrm{TO}}/I_{\mathrm{LO}}$ value (I_{TO}: peak intensity of InSb TO mode; I_{LO}: peak intensity of InSb LO mode), indicating good crystal orientation (Fig. 2b and Table 1b). Furthermore, the second-order InSb LO mode (2LO) appeared at Bi content $x = 0.02$ and 0.03 (insets (i) and (ii) in Fig. 2b) [29]. The appearance of this peak suggested a large increase in the crystallinity. On the other hand, the peak intensities in the region marked with an asterisk decreased with increasing growth rate in the InSb/PI (Fig. 2c) and the FWHM of the dominant phonon mode (InSb TO mode) was almost unchanged (Table 1c). For the thin films grown on PI films, a parameter for the degree of crystallization was defined as $(I_{\mathrm{TO}} + I_{\mathrm{LO}})/\left(I_{A_{1\mathrm{g}}} + I_a\right)$, where $I_{A_{1\mathrm{g}}}$was the peak intensity of the $A_{1\mathrm{g}}$ mode of the Sb cluster and I_a was the intensity of the peak that originated from amorphization. The crystallization degree of the InSb/PI was higher at high growth rates (Table 1c), owing to the suppression of amorphization and of Sb cluster formation. Bi doping increased the crystallinity of the $InSb_{1-x}Bi_x$/PI (Fig. 2d and Table 1d). In particular, the InSb TO mode peak intensity and the crystallization degree increased considerably at Bi content $x = 0.03$.

The behavior of Bi in the InSb thin films was analyzed from the XRD patterns and Raman spectra. In the thin films grown on quartz substrates, the 2LO Raman peak, which indicates good crystallinity, was observed at Bi content $x = 0.02$ and 0.03, even though Bi cluster diffraction peaks were observed. On the other hand, the preferred orientation changed from (220) to (111) as the Bi content x increased in the $InSb_{1-x}Bi_x$/PI. Although Bi clusters were formed at Bi content $x = 0.03$, the crystallization of thin films was increased by suppressing amorphization and Sb cluster formation. This observation suggests that the structural disorder in InSb thin films disturbs the (111)-oriented growth, similar to the solid phase growth of polysilicon [27]. In addition, the grain size of the thin films was increased by Bi doping (Fig. 3). The accuracy of grain sizes obtained by using XRD pattern analysis was confirmed by comparing the grain sizes of the InSb/quartz, which had the smallest dispersion (Fig. 3a), with those of the InSb/quartz obtained by surface morphology analysis (Fig. 3c). These results revealed that the crystallinity of flexible InSb thin films was improved by Bi doping.

3.2 Stacking-fault probability

For strain- and defect-free polycrystals, the plot of the lattice parameter against the diffractometer function, $f(\theta) = \cos\theta\cot\theta$, is linear. The lattice parameter, a_{HKL}, is

derived from the diffraction angle, θ_{HKL}, in the XRD pattern. Here, H, K, and L are defined as the integer multiples of Miller indices (hkl), respectively. Considering the strain and stacking-faults in fcc metals and semiconductor thin films, the stacking-fault probabilities were evaluated by [18–20]

$$a_{HKL} = a_0 + mf(\theta_{HKL}) + a_0\varepsilon_{(hkl)}^{zz} + a_0\left(G_{HKL} + \varepsilon_{(hkl)}^{SF}J_{HKL}\right)\alpha_{(hkl)}^{SF}, \quad (1)$$

where a_0 is the lattice constant (InSb: 6.479 Å), m is a constant, and $\varepsilon_{(hkl)}^{SF}$ is the fractional change in interplanar spacing at the stacking-fault. $\alpha_{(hkl)}^{SF}$, which is $\alpha_{(hkl)}^{ISF} - \alpha_{(hkl)}^{ESF}$, is the net stacking-fault probability ($\alpha_{(hkl)}^{ISF}$: intrinsic stacking-fault probability; $\alpha_{(hkl)}^{ESF}$: extrinsic stacking-fault probability). $\varepsilon_{(hkl)}^{zz}$ is the strain vertical to the substrate, which is caused by the difference in thermal expansion coefficients between the substrate and the (hkl)-oriented crystal grains in the thin film. Generally, the strain of polycrystalline thin films is easily relaxed. The strain of thin films has been analyzed by using the Raman peak shift [30]. In the Raman spectra of the thin films (Fig. 2), the InSb TO mode peak position was the same in the InSb/quartz, $InSb_{1-x}Bi_x$/quartz, and InSb/PI, suggesting that these thin films had almost no strain. Consequently, it was unnecessary to consider $\varepsilon_{(hkl)}^{zz}$ in Eq. 1. However, the Raman peak shift showed that $InSb_{1-x}Bi_x$/PI had tensile strain. This is due to the increased grain size on PI films with activated surface by reverse sputtering. The $\varepsilon_{(hkl)}^{zz}$ values for the $InSb_{1-x}Bi_x$/PI were determined based on the

work of Anastassakis, who calculated the strain of epitaxially grown thin films in arbitrary directions [31].

$$\varepsilon_{(hkl)}^{zz} = \varepsilon^{\perp} = \varepsilon^{\parallel} - \varepsilon^{\parallel}\Delta\tilde{\varepsilon}. \qquad (2)$$

The reduced tetragonal distortion, $\Delta\tilde{\varepsilon}$, is defined for any direction [31]. The in-plane thermal strain is expressed as [20]

$$\varepsilon^{\parallel} = \varepsilon^{xx} = \varepsilon^{yy} = \left(\alpha_{\mathrm{InSb}}^{th} - \alpha_{\mathrm{PI}}^{th}\right)\Delta T, \qquad (3)$$

where $\alpha_{\mathrm{InSb}}^{th}$ and $\alpha_{\mathrm{PI}}^{th}$ are the thermal expansion coefficients of InSb (5.5×10^{-6} °C^{-1}: [32]) and the PI film (2.0×10^{-5} °C^{-1}: [33]), respectively. ΔT (= 300 °C) is the difference between room temperature and the growth temperature.

Fig. 4 shows a_{HKL} plotted against $f(\theta) = \cos\theta\cot\theta$. The solid lines show $a_0 + mf(\theta_{HKL})$ in the strain- and defect-free state. In Fig. 4a and b, m (= -0.0015) was determined by fitting the plots of three InSb/quartz using the least-squares method. The deviation of a_{HKL} from the linear relation reduces with Bi doping. On the other hand, the structural disorder of the thin films grown on PI films was high, except for $InSb_{0.97}Bi_{0.03}$ (Fig. 2c and d). m is decided from unstrained perfect polycrystalline material. For this reason, m (= 0.0012) was determined in Fig. 4c and d by fitting the plots of a_{HKL} without the strain component of $InSb_{0.97}Bi_{0.03}$/PI ($a_{HKL} - a_0\varepsilon_{(hkl)}^{zz}$: open circles in Fig. 4d3) by using the least-squares method. The deviation of the plotted values

of a_{HKL} from the linear relation in the InSb/PI (Fig. 4c) was larger than those of the InSb/quartz (Fig. 4a): the structural disorder in the InSb/PI was high. The plots of $a_{HKL} - a_0\varepsilon_{(hkl)}^{zz}$ (open symbols in Fig. 4d) agreed more closely with the linear relation as the Bi content x increased.

The preferred orientation was (111) in the thin films with some structural disorder. Owing to this result, the stacking-fault probability was estimated for the (111) orientation. Among the $InSb_{1-x}Bi_x$/PI, only the $InSb_{0.97}Bi_{0.03}$/PI with a good crystallization degree was subjected to the stacking-fault probability analysis because $InSb_{1-x}Bi_x$/PI with Bi content $x = 0.01$ and 0.02 contained types of structural disorder other than stacking-faults. The deviation from the linear relation, Δa_{HKL}, is proportional to stacking-fault probability (Eq. 4).

$$\Delta a_{HKL} = a_{HKL} - a_0 - mf(\theta_{HKL}) - a_0\varepsilon_{(hkl)}^{zz} = a_0\left(G_{HKL} + \varepsilon_{(hkl)}^{SF}J_{HKL}\right)\alpha_{(hkl)}^{SF}. \quad (4)$$

Accordingly, $\alpha_{(111)}^{SF}$ and $\varepsilon_{(111)}^{SF}$ can be estimated by solving the following simultaneous equations:

$$\Delta a_{111} = a_0\left(G_{111} + \varepsilon_{(111)}^{SF}J_{111}\right)\alpha_{(111)}^{SF}, \quad (5)$$

$$\Delta a_{333} = a_0\left(G_{333} + \varepsilon_{(111)}^{SF}J_{333}\right)\alpha_{(111)}^{SF}. \quad (6)$$

Here, G_{111}, G_{333}, J_{111}, and J_{333} are -0.0345, 0.0029, 0.209, and 0.010, respectively [18]. The growth rate dependencies for $\alpha_{(111)}^{SF}$ and $\varepsilon_{(111)}^{SF}$ are shown in Fig. 5a and b,

respectively. In the thin films grown on quartz substrates, the absolute values for $\alpha_{(111)}^{SF}$ were decreased by Bi doping (Fig. 5a), whereas $\varepsilon_{(111)}^{SF}$ was almost unchanged (Fig. 5b). In addition, at Bi content $x = 0.03$, $\alpha_{(111)}^{SF}$ and $\varepsilon_{(111)}^{SF}$ of the thin films grown on PI films were suppressed to the same levels as those of the thin films grown on quartz substrates (closed triangle in Fig. 5a and closed diamond in Fig. 5b).

3.3 Environment resistance and cytotoxicity of InSb and $InSb_{0.97}Bi_{0.03}$ thin films

The effects of crystallinity improvement of InSb thin films by Bi doping on chemical stability under aqueous conditions and on cytotoxicity were assayed. According to our previous studies [4,11], InSb and $InSb_{0.97}Bi_{0.03}$ thin films were soaked in pH 5 buffer for 14 days and the concentration of In eluted in the buffer was determined by MP-AES. Fig. 6a shows the total amount of In eluted from InSb and $InSb_{0.97}Bi_{0.03}$ thin films grown on quartz substrates and PI films. Elution of In from grown thin films did not affected by the substrate, and Bi doping prevented In elution. Following 14 days immersion in pH 5 buffer, the InSb thin films were all dissolved, whereas the $InSb_{0.97}Bi_{0.03}$ thin films remained on both the quartz substrate and PI film (photographs in Fig. 6a). Fig. 6b shows the fluorescence imaging live/dead assay results, in which living cells are stained green and dead cells are stained red. InSb and $InSb_{0.97}Bi_{0.03}$ thin films on PI films

were soaked in 20 mL of culture medium for 24 h at room temperature and L929 cells were exposed to the test solution for 24 h. There were slightly fewer dead cells and more living cells for the $InSb_{0.97}Bi_{0.03}$ thin film than for the InSb thin film. These results suggest that Bi doping can enhance the environmental stability and lower the cytotoxicity of InSb.

4 Conclusions

InSb and $InSb_{1-x}Bi_x$ thin films were grown on quartz substrates and PI films. The properties of the InSb/PI were inferior to those of the InSb/quartz because the crystallinity of the InSb/PI was low due to the structural disorder caused by the lack of crystal growth driving force. The crystallinity of InSb thin films was improved by Bi doping. In particular, the increase in crystallinity for the $InSb_{1-x}Bi_x$/PI was remarkable and the properties of the $InSb_{0.97}Bi_{0.03}$/PI were comparable to those of the InSb/quartz and $InSb_{1-x}Bi_x$/quartz. Furthermore, the environmental stability of the InSb thin films was enhanced by Bi doping. We believe that the improvements in the properties of these flexible thin films by Bi doping can contribute to realizing the United Nations' Sustainable Development Goals.

Declarations

There are no conflicts of interest to declare.

References

[1] J.D. Sachs, G. Schmidt-Traub, M. Mazzucato, D. Messner, N. Nakicenovic, J. Rockström, Nat. Sustain. **2**, 805–814 (2019). https://doi.org/10.1038/s41893-019-0352-9.

[2] Y. Suzuki, S. Iwashita, T. Sato, H. Yonemichi, H. Moki, T. Moriya, 2018 International Symposium on Semiconductor Manufacturing (ISSM), 2018, pp. 1–4. https://doi.org/10.1109/ISSM.2018.8651142.

[3] E. Hille, W. Althammer, H. Diederich, Technol. Forecasting Social Change **153**, 119921 (2020). https://doi.org/10.1016/j.techfore.2020.119921.

[4] N. Nishimoto, J. Fujihara, Phys. Status Solidi A **216**, 1800860 (2019). https://doi.org/10.1002/pssa.201800860.

[5] Z. Lou, G. Shen, Small Struct. **2**, 2000152 (2021). https://doi.org/10.1002/sstr.202000152.

[6] C. Zeng, A. Gonzalez-Alvarez, E. Orenstein, J.A. Field, F. Shadman, R. Sierra-Alvarez, Ecotoxicol. Environ. Saf. **140**, 30–36 (2017). http://dx.doi.org/10.1016/j.ecoenv.2017.02.029.

[7] L. Ye, S. Qiu, X. Li, Y. Jiang, C. Jing, Sci. Total Environ. **640–641**, 1–8 (2018). https://doi.org/10.1016/j.scitotenv.2018.05.267.

[8] M.A. Arshad, H.M. Ebeid, F. Hassan, Biol. Trace Elem. Res. **199**, 3319–3337 (2021). https://doi.org/10.1007/s12011-020-02480-6.

[9] M. Kamiko, K. Aotani, R. Suenaga, J.-W. Koo, J.-G. Ha, Vacuum **86**, 438–442 (2011). https://doi.org/10.1016/j.vacuum.2011.09.004.

[10] J. Schmidt, D. Tetzlaff, E. Bugiei, T.F. Wietler, J. Cryst. Growth **457**, 171–176 (2017). https://doi.org/10.1016/j.crysgro.2016.06.053.

[11] N. Nishimoto, J. Fujihara, Mater. Chem. Phys. **274**, 125160 (2021). https://doi.org/10.1016/j.matchemphys.2021.125160.

[12] C.A. Bolzan, B. Johannessen, Z. Wu, R. Giulian, Solid State Sci. **119**, 106705 (2021). https://doi.org/10.1016/j.solidstatesciences.2021.106705.

[13] S.B. Touski, Superlattices. Microstruct. **156**, 106979 (2021). http://doi.org/10.1016/j.spmi.2021.106979.

[14] D.N. Gupta, Plasmonics **16**, 419–424 (2021). https://doi.org/10.1007/s11468-020-

01291-8.
[15] S.W. Jun, R.T. Lee, C.M. Fetzer, J.K. Shurtleff, G.B. Stringfellow, C.J. Choi, T.-Y. Seong, J. Appl. Phys. **88**, 4429–4433 (2000). https://doi.org/10.1063/1.1289478.
[16] S. Tixier, M. Adamcyk, E.C. Young, J.H. Schmid, T. Tiedje, J. Cryst. Growth **251**, 449–454 (2003). https://doi.org/10.1016/S0022-0248(02)02217-0.
[17] P. Ludewig, Z.L. Bushell, L. Nattermann, N. Knaub, W. Stolz, K. Volz, J. Cryst. Growth **396**, 95–99 (2014). https://doi.org/10.1016/j.jcrysgro.2014.03.041.
[18] R.P.I. Adler, C.N.J. Wagner, Metall. Mater. Trans. B **1**, 2791–2797 (1970). https://doi.org/10.1007/BF03037816.
[19] N. Kuwano, Y. Tomokiyo, C. Kinoshita, T. Eguchi, Trans. Jpn. Inst. Met. **15**, 338–344 (1974). https://doi.org/10.2320/matertrans1960.15.338.
[20] Y. Kajikawa, Y. Iseki, Y. Matsui, IPRM 2011 - 23rd International Conference on Indium Phosphide and Related Materials, 2011, pp. 1–3.
[21] H. Toraya, J. Appl. Cryst. **51**, 446–445 (2018). https://doi.org/10.1107/S1600576718001474.
[22] P.P. Murmu, J. Levenur, J.G. Storey, J. Kennedy, Materials Today: Proceedings **36**, 416–420 (2021). https://doi.org/10.1016/j.matpr.2020.04.752.
[23] D. Bhusari, H. Hayden, R. Tanikella, S.A.B. Allen, P.A. Kohl, J. Electrochem. Soc. **152**, F162–F170 (2005). https://doi.org/10.1149/1.2006587.
[24] M. Imaizumi, M. Adachi, Y. Fujii, Y. Hayashi, T. Soga, T. Jimbo, M. Umeno, J. Cryst. Growth **221**, 688–692 (2000). https://doi.org/10.1016/S0022-0248(00)00801-0.
[25] A. Iribarren, R. Castro-Rodríguez, L. Ponce-Cabrera, J.L. Peña, Thin Solid Films **510**, 134–137 (2006). https://doi.org/10.1016/j.tsf.2005.12.302.
[26] D. Song, D. Inns, A. Straub, M.L. Terry, P. Campbell, A.G. Aberle, Thin Solid Films **513**, 356–363 (2006). https://doi.org/10.1016/j.tsf.2006.01.010.
[27] X. Zhang, T.-Y. Zhang, M. Wong, Y. Zohar, J. Microelectromech. Syst. **7**, 356–364 (1998). https://doi.org/10.1109/84.735342.
[28] I. Zardo, S. Conesa-Boj, F. Peiro, J.R. Morante, J. Arbiol, E. Uccelli, G. Abstreiter, A. Fontcuberta i Morral, Phys. Rev. B **80**, 245324 (2009). https://doi.org/10.1103/PhysRevB.80.245324.
[29] K.P. Lim, H.T. Pham, S.F. Yoon, C.Y. Ngo, S. Tripathy, Appl. Phys. Lett. **96**,

161903 (2010). https://doi.org/10.1063/1.3399775.

[30] C.A. Taylor, M.F. Wayne, W.K.S. Chiu, Thin Solid Films **429**, 190–200 (2003). https://doi.org/10.1016/S0040-6090(03)00276-1.

[31] E. Anastassakis, J. Cryst. Growth **114**, 647–655 (1991). https://doi.org/10.1016/0022-0248(91)90411-W.

[32] X. Cai, J. Wei, J. Appl. Phys. **114**, 083507 (2013). https://doi.org/10.1063/1.4819224.

[33] A.S. Hicyilmaz, A.C. Bedeloglu, SN Appl. Sci. **3**, 363 (2021). https://doi.org/10.1007/s42452-021-04362-5.

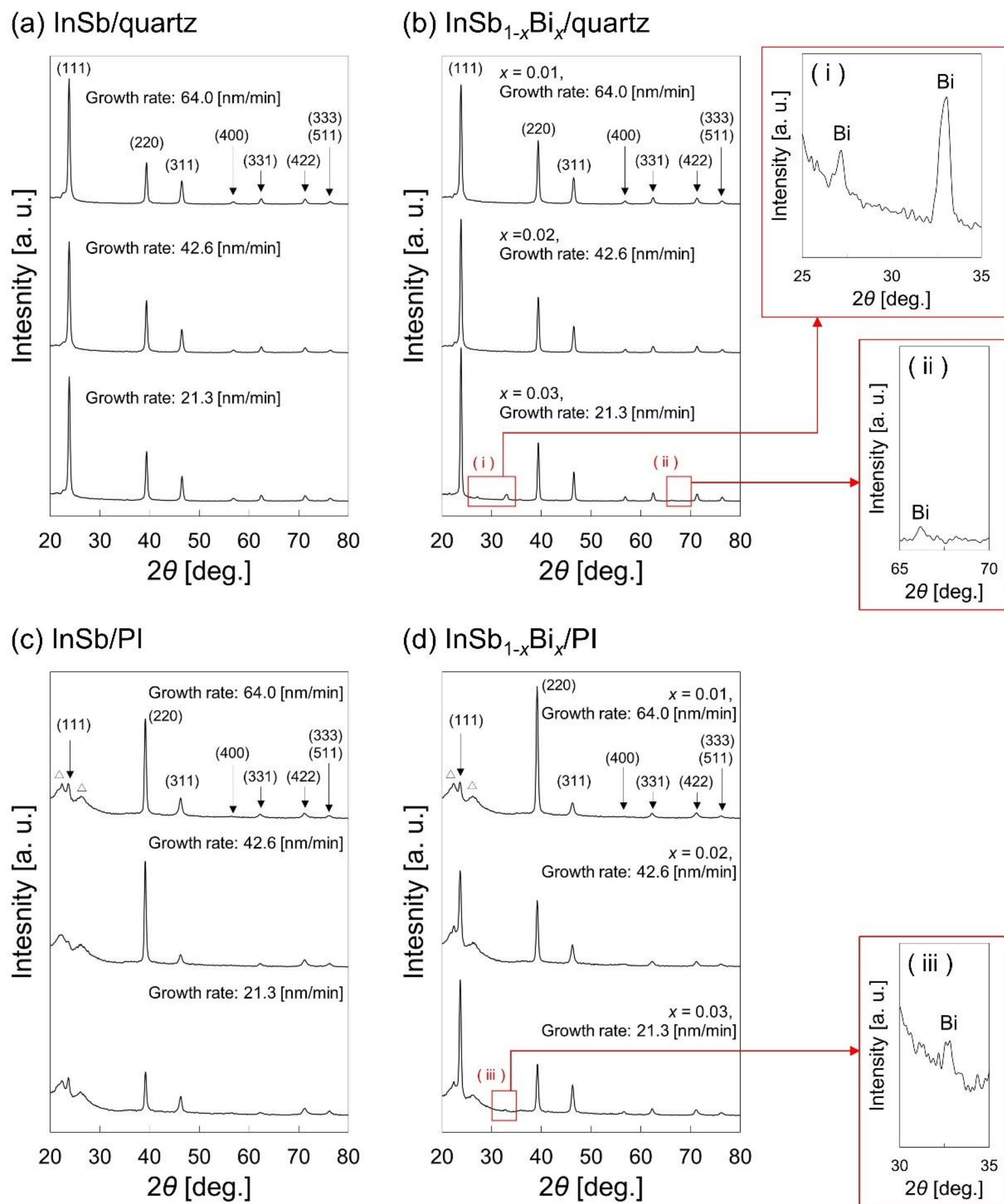

Fig. 1. XRD patterns at different growth rates and Bi contents x for (a) InSb/quartz, (b) $InSb_{1-x}Bi_x$/quartz, (c) InSb/PI, and (d) $InSb_{1-x}Bi_x$/PI. The broad diffraction peaks around 22° and 26° (open triangles) are attributed to the PI film. Insets (i)–(iii) show details of the spectra.

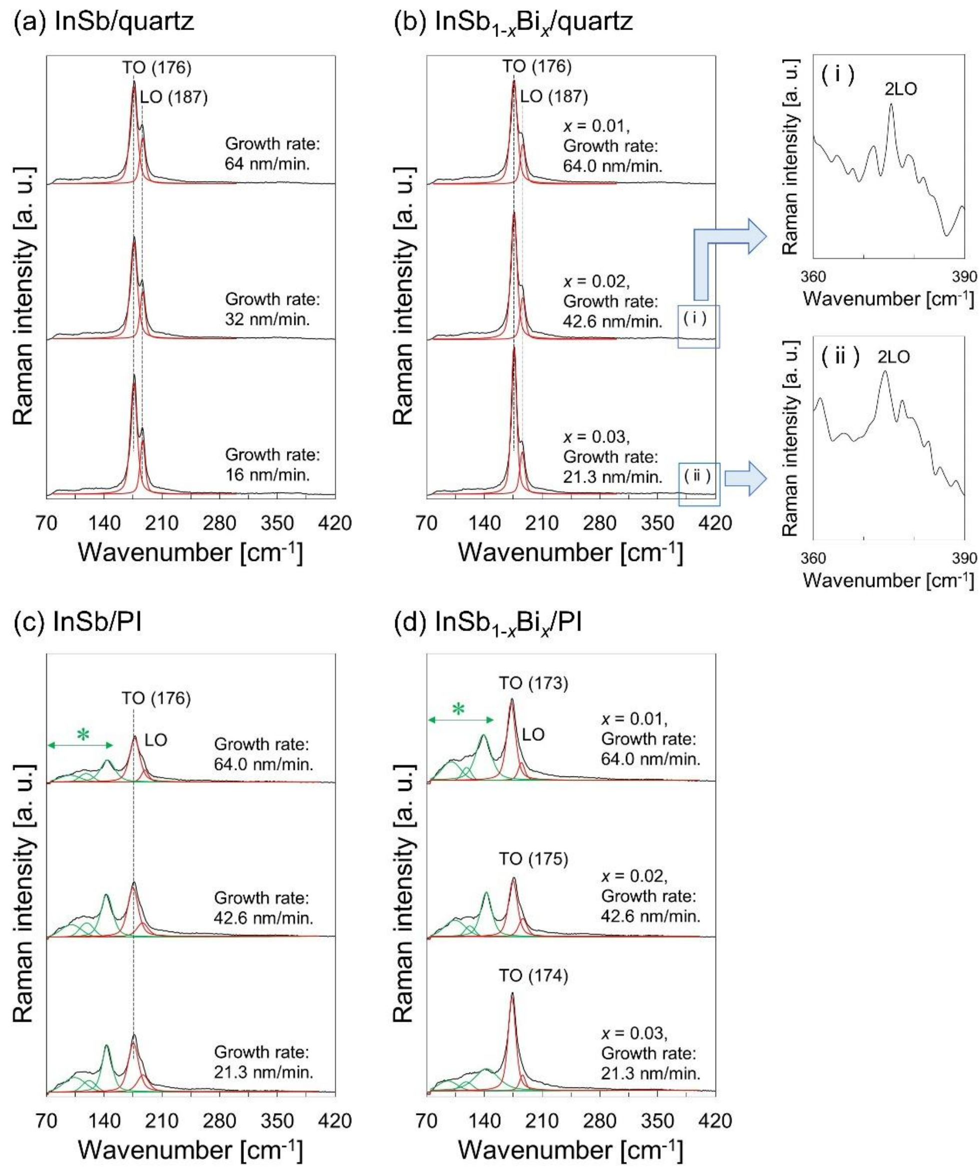

Fig. 2. Raman spectra at different growth rates and Bi contents x for (a) InSb/quartz, (b) $InSb_{1-x}Bi_x$/quartz, (c) InSb/PI, and (d) $InSb_{1-x}Bi_x$/PI. The red solid curves show the results of the curve fitting analysis for the InSb TO and LO mode peaks and the green solid curves show those for the peaks originating from structural disorder (region *). Insets (i) and (ii) show details of the spectra.

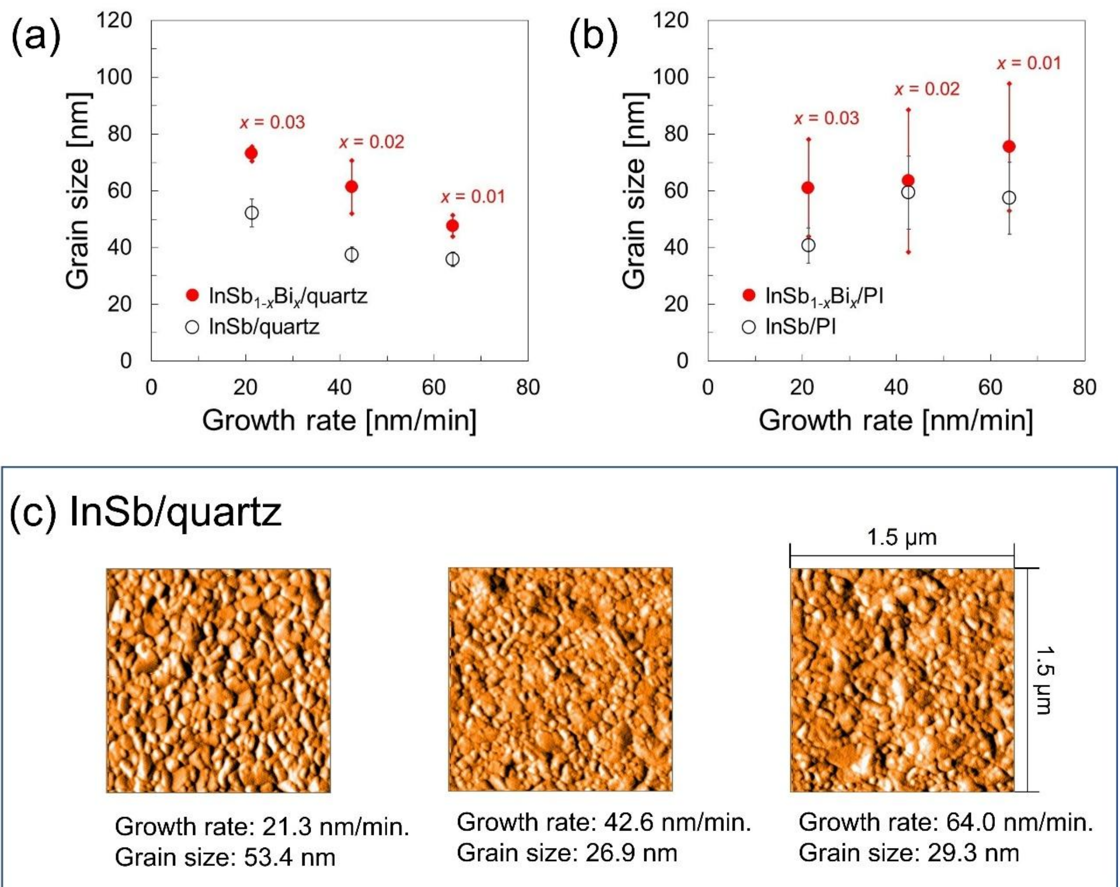

Fig. 3. Grain sizes at different growth rates and Bi contents x of InSb and $InSb_{1-x}Bi_x$ thin films on (a) quartz substrates and (b) PI films. (c) Surface morphologies of InSb/quartz.

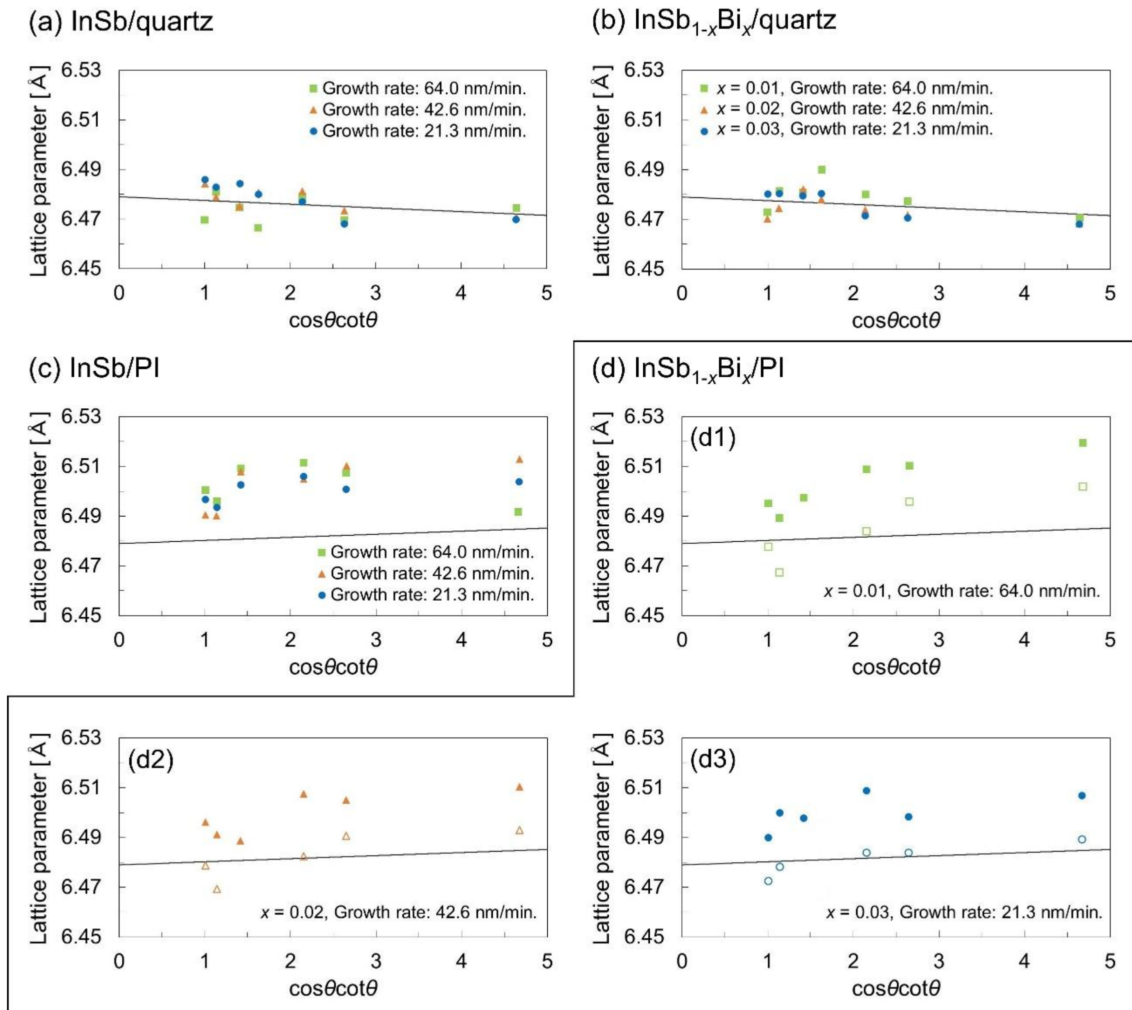

Fig. 4. Lattice parameters at various growth rates and Bi contents x as a function of $\cos\theta\cot\theta$ for (a) InSb/quartz, (b) $InSb_{1-x}Bi_x$/quartz, (c) InSb/PI, and (d) $InSb_{1-x}Bi_x$/PI. Closed symbols represent a_{HKL} and open symbols represent a_{HKL} without the strain component ($a_{HKL} - a_0\varepsilon_{(hkl)}^{zz}$) of $InSb_{1-x}Bi_x$/PI.

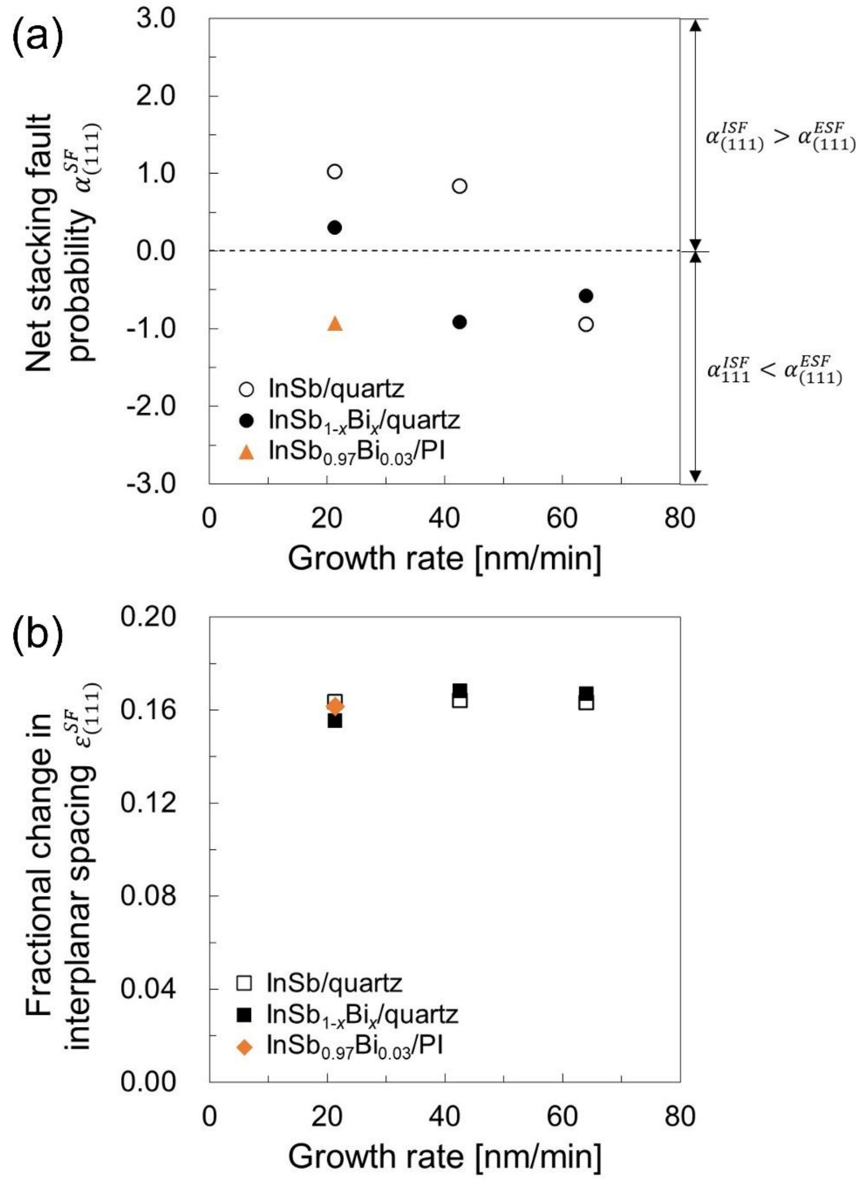

Fig. 5. Estimated (a) net stacking fault probability $\alpha_{(111)}^{SF}$ and (b) fractional change in interplanar spacing $\varepsilon_{(111)}^{SF}$ as a function of growth rate.

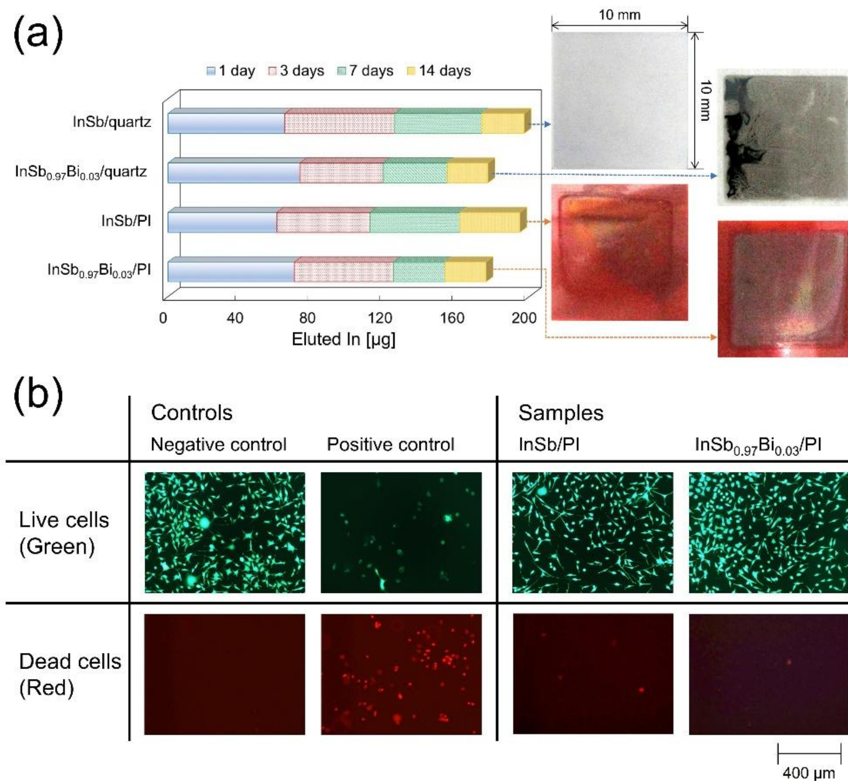

Fig. 6. (a) Total amount of In eluted from InSb and $InSb_{0.97}Bi_{0.03}$ thin films grown on quartz substrates and PI films. InSb and $InSb_{0.97}Bi_{0.03}$ thin films were soaked in pH 5 buffer for 14 days and the concentration of In eluted in the buffer was determined by MP-AES. Photographs of the films are shown on the right-hand side. (b) Fluorescence images of L929 cells treated with Live/Dead cell staining solution. Green indicates live cells and red indicates dead cells. L929 cells were plated on a six-well plate. The test solution was prepared by soaking InSb thin films in culture medium for 24 h, and then the solutions were added to the wells for 24 h. Negative controls were prepared without adding test solution, and 0.2% Tween 20 was added to the positive control.

Table 1. Numerical data for Raman spectra analysis by curve fitting of (a) InSb/quartz, (b) $InSb_{1-x}Bi_x$/quartz, (c) InSb/PI, and (d) $InSb_{1-x}Bi_x$/PI.

Quartz substrate						
Film composition		Growth rate [nm/min]	FWHM [cm^{-1}] TO mode	FWHM [cm^{-1}] LO mode	I_{TO}/I_{LO}	ω_{2LO} [cm^{-1}]
(a)	InSb	64.0	10.4	7.7	2.1	—
		42.6	10.2	7.3	2.1	—
		21.3	9.7	7.1	2.1	—
(b)	$InSb_{0.99}Bi_{0.01}$	64.0	9.8	7.3	2.6	—
	$InSb_{0.98}Bi_{0.02}$	42.6	9.0	7.3	3.0	375
	$InSb_{0.97}Bi_{0.03}$	21.3	7.7	7.3	3.5	375

PI film						
Film composition		Growth rate [nm/min]	FWHM [cm^{-1}] TO mode	FWHM [cm^{-1}] LO mode	I_{TO}/I_{LO}	$(I_{TO}+I_{LO})/\left(I_{A_{1g}}+I_a\right)$
(c)	InSb	64.0	14.7	10.0	3.7	1.9
		42.6	15.2	16.2	3.5	1.2
		21.3	15.1	16.4	2.9	1.1
(d)	$InSb_{0.99}Bi_{0.01}$	64.0	12.6	9.3	4.4	1.5
	$InSb_{0.98}Bi_{0.02}$	42.6	12.9	12.1	3.1	1.0
	$InSb_{0.97}Bi_{0.03}$	21.3	11.2	8.5	6.0	3.4

I_{TO} and I_{LO} are the peak intensities of the TO mode and LO mode, respectively. ω_{2LO} is the wavenumber of the second-order LO peak. $I_{A_{1g}}$ is the peak intensity of the A_{1g} mode of the Sb cluster, and I_a is the intensity of the peak due to amorphization.